

# Minimum Radiative Heat and Propellant Aerocapture Guidance with Attitude Kinematics Constraints\*

Enrico M. Zucchelli <sup>†</sup>

*Massachusetts Institute of Technology, Cambridge, MA, 02139*

Erwin Mooij <sup>‡</sup>

*Delft University of Technology, Delft, 2629 HS, The Netherlands*

To maximize the payload mass, an aerocapture trajectory should be flown in such a way that both the final  $\Delta V$  and the total heat load are minimized. For some aerocapture missions, the heating due to radiation of high temperature gases in the shock-layer is so much larger than the heat due to convection, that the latter is negligible. This paper provides analytical proof and numerical validation that radiative heat is minimized by the same trajectory that minimizes the final  $\Delta V$ : a single switch bang-bang trajectory, starting with full lift-up, full lift-down commands. Further, a novel guidance that plans a bang-bang trajectory with constraints in the attitude kinematics is introduced. While achieving similar performance as the current state-of-the-art, the inclusion of constraints in attitude kinematics allows for much less tuning. Finally, a lateral guidance that makes use of information on the final inclination of the predicted trajectory is introduced. Such guidance allows for very high accuracy in the inclination requirements with only two reversals, by requiring a single parameter to be tuned.

## Nomenclature

$a$	orbital semi-major axis, m
$C_D$	drag coefficient
$C_L$	lift coefficient
$D$	drag, N
$e$	orbital eccentricity
$g_\delta$	latitudinal component of the gravity, $m/s^2$
$g_r$	radial component of the gravity, $m/s^2$
$i$	orbital inclination, rad
$L$	lift, N

---

\*An initial version of this paper was presented at the 2018 AIAA Guidance, Navigation, and Control Conference, 8-12 January 2018, Kissimmee, Florida. Paper number AIAA 2018-1319.

<sup>†</sup>Postdoctoral Associate, Aeronautics and Astronautics, 77 Massachusetts Avenue, AIAA Member.

<sup>‡</sup>Associate Professor, Aerospace Engineering, Kluyverweg 1, Associate Fellow AIAA.

$m$	mass, kg
$\dot{q}$	heat flux at stagnation point, W/s <sup>2</sup>
$Q$	integrated heat load, J/s <sup>2</sup>
$r$	radial distance, m
$R_e$	equatorial radius of the Earth, m
$R_N$	nose radius, m
$t$	time, s
$V$	relative speed, m/s
$\beta$	inverse of scale-height, 1/m
$\gamma$	relative flight-path angle, rad
$\delta$	latitude, rad
$\lambda$	co-state
$\mu$	gravitational parameter of the Earth, m <sup>3</sup> /s <sup>2</sup>
$\rho$	atmospheric density, kg/m <sup>3</sup>
$\sigma$	bank angle, rad
$\tau$	longitude, rad
$\chi$	heading, rad
$\omega_{cb}$	rotational rate of the Earth, rad/s

*Subscripts*

0	initial conditions
$a$	apoapsis
$m$	margin
$p$	periapsis
$pred$	end of prediction
$rev$	reversal
opt	optimal

*Superscripts*

★	target
---	--------

## I. Introduction

Aerocapture, first introduced by Cruz [1], is an atmospheric maneuver that can greatly facilitate missions to atmospheric celestial bodies [2]. Aerocapture achieves orbit insertion from a hyperbolic trajectory, as depicted in Fig. 1. By diving into the atmosphere, the energy of the spacecraft is reduced in a controlled way through the dissipative action of drag. After the desired amount of energy has been lost, the spacecraft exits the atmosphere and coasts to apoapsis. A small propulsive burn is then required to raise the periapsis above the region where drag is still significant. If needed a second smaller burn is later performed to correct any errors in the target apoapsis altitude.

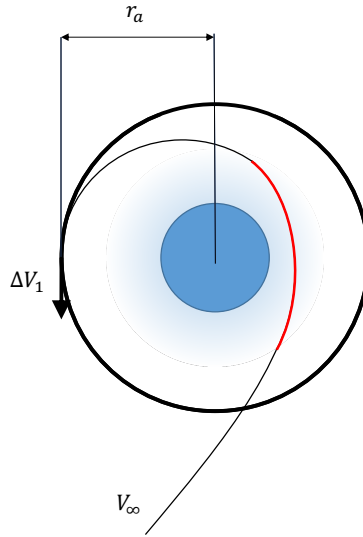


**Fig. 1 Scheme of an aerocapture. In red is the atmospheric part of the maneuver.**

An aerocapture maneuver has never been attempted, despite most of the technology being considered ready by several studies now [3–5]. Interest in aerocapture has lately been growing lately as it would be an enhancing technology for mission to Neptune and Uranus planets [6–8]; specifically, attractiveness comes from the fact that it would allow faster, higher energy trajectories, since less propellant mass would be required to decelerate. The mass reduction granted by decreased propellant consumption is partially offset by the requirement of a heat shield to protect the spacecraft while entering the atmosphere. Because of the extremely high temperatures encountered during this class of maneuvers, the heat shield is generally ablative, meaning that the mass increases for larger total heat load. Hence, an optimal aerocapture should not only minimize the  $\Delta V$  of the post-maneuver burns, but strike a balance between total heat load and total propellant consumption. The minimum  $\Delta V$  aerocapture follows a bang-bang trajectory, beginning with a full lift-up command, and with a single switch [9, 10]. The trajectory minimizing the  $\Delta V$  also minimizes both the heat flux peak and the peak dynamic pressure [11]. However such a trajectory *maximizes* the integrated convective heat, which is in turn minimized by a bang-bang trajectory that begins with a full lift-down command [12].

A large source of heat during atmospheric missions is due to the radiation of high-temperature gases in the shock

layer [13, 14]. For lunar return aerocapture, which is the lowest speed aerocapture possible on Earth, heat load due to convection and heat load due to radiation are comparable in magnitude for trajectories flown by Orion. At higher initial velocities, the radiative heat load becomes increasingly more important, since it generally grows faster than convective heat at higher speeds. Further, heat flux due to radiation increases with increasing nose radius, whereas the opposite happens for convective heat flux, making radiative heat dominant for larger spacecraft. The density, composition, and scale height of the atmosphere also affect the ratio between the two components of the heat; for example, radiative heat is generally negligible for missions to Uranus [15], may be relevant on Mars depending on entry velocity [16], and is instead expected to be the major source of heat for missions to Neptune and Titan [17–19]. The first key contribution of this paper is to analytically prove, given a few assumptions, that the minimum radiative heat load aerocapture trajectory coincides with the trajectory minimizing the  $\Delta V$ . The proof encompasses many of the several empirical radiative heat formulations that have been proposed in the last 40 years. The proof is validated numerically for a variety of conditions and formulations of radiative heat flux. The same proof can be used to deduce the fact that convective heat is instead maximized by that trajectory, as previously shown by Sigal and Guelman [12]; however, this proof generalizes to more empirical formulations of convective heat flux than the one considered by Sigal and Guelman. Finally, for cases where the heat due to convection is negligible compared to radiative heat, the same trajectory can minimize  $\Delta V$  and total heat load at the same time, avoiding the need to seek trade-offs.

To fly the minimum heat, minimum  $\Delta V$  aerocapture, this paper introduces a novel optimal numerical predictor-corrector (NPC) guidance. Initial efforts to develop an optimal guidance for aeroassisted maneuvers focused on orbital plane change with minimum energy loss [20–22]. Early Aerocapture guidance schemes were derived from the Apollo skip entry guidance [23] which relies on the tracking of a nominal trajectory. Aerocapture NPCs seek a constant bank angle to be kept throughout the entirety of the trajectory [24] such that the desired apoapsis is targeted. Optimal aerocapture guidance was initially proposed to minimize the control effort [20]. Optimality for closed-loop guidance in terms of  $\Delta V$  for an aeroassisted maneuver was later considered by Evans and Dukeman for aerobraking [25]. The minimum  $\Delta V$  is obtained by maximizing exit velocity for a given apoapsis. To this end, the algorithm is divided into two phases. In the first phase, the algorithm integrates the trajectory with a constant, quasi full lift-down bank angle. If the predicted apoapsis is lower than the target one, full lift-up is commanded; else, Phase 2 is triggered, in which the algorithm then behaves like the guidance in Ref. [24]. This approach achieves optimality avoiding online trajectory optimization. A bank angle margin is required, which decreases performance, but reduces the risk of skipping out. Bank angle margins are constant independently of the entry conditions. This choice leads to a decrease in performance for shallow entry angles. An improvement to the approach is the Fully Numerical Predictor-corrector Aerocapture Guidance (FNPAG) [10] for aerocapture. Performance is improved by tuning the optimal bank angle margins as a function of entry angle and velocity. The parameter is tuned for a two-dimensional grid of different entry conditions; for each point of the grid, Monte Carlo runs are required for the tuning. At the beginning of the maneuver, the parameter

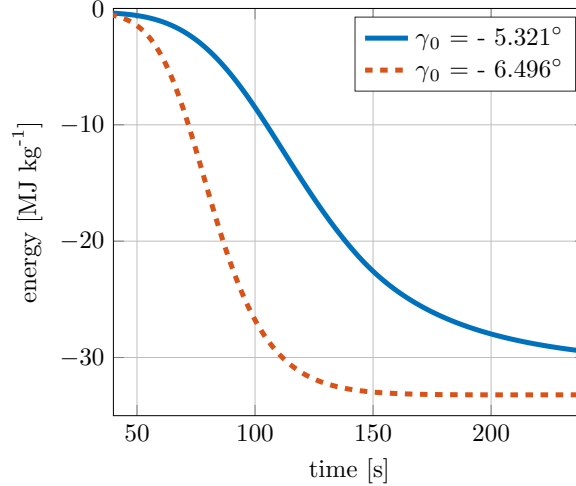


**Fig. 2 Specific energy versus time for aerocapture flow with constant bank angle.**

is interpolated from the grid. Recent developments have been considering uncertainties directly in the planning via stochastic and robust optimization under uncertainty, similarly to stochastic model predictive control [26, 27], or with two stage optimization under uncertainty [28], for cases where perturbations are so large that there is no control profile that leads to feasible trajectory under all perturbations. Whilst these approaches are more robust than the FNPAG, they are also more computationally demanding. On the other hand, common alternatives to NPCs are analytical predictor-correctors (APCs) [29–32], which make more simplifications than NPCs, and result in a faster, but potentially less robust, guidance algorithm.

This paper improves on the FNPAG by showing that the major reason why different bank angle margins are needed for different entry conditions is the unconstrained kinematics in the motion planning during Phase 1. Taking the kinematics into account makes the planning more robust and easier to tune. The rotation from the bank angle of Phase 1 to the bank angle of Phase 2 occurs instantaneously in the planning of the guidance logics of Refs. [10] and [25]. In fact, for the majority of re-entry guidance systems, attitude kinematics are not taken into account while planning, and their effect is usually negligible. A rotation from full lift-up to full lift-down may take more to 15 seconds, which is short relatively to the entirety of an atmospheric re-entry flight. During aerocapture however, 15 seconds are enough to dissipate more than 30% of the difference in energy between initial and final states, as shown in Fig. 2. The percentage is strongly dependent on the initial flight path angle and velocity, which affect both the overall duration of the maneuver and the switching time. Therefore, a predictor-corrector guidance for aerocapture is greatly benefited by including the effects of this rotation in the prediction. The guidance proposed in this paper takes attitude kinematics constraints into account. As a result, it performs similarly to that of Ref. [10], but using the minimal tuning of Ref. [25].

The proposed longitudinal guidance is complemented by a novel robust lateral guidance. The lateral guidance aims to minimize the number of bank reversals. It does so by predicting the trajectory as if a bank reversal was happening

immediately, and, similarly to the longitudinal guidance, it includes attitude kinematics constraints. This allows the lateral guidance to take into account several perturbations induced by the reversal, such as the finite time of the bank reversal, and the effect of accelerations that depend on the heading or on the position of the spacecraft, such as Coriolis. The proposed lateral guidance has been partly tailored to the longitudinal guidance proposed in this paper, but is easily applicable to other entry problems.

The contributions of this paper can be summarized as follows:

- The analytical proof that the minimum radiative heat load aerocapture is the same trajectory that leads to a minimum  $\Delta V$ . For very high-speed aerocapture, convective heat flux is much smaller than radiative heat flux; thus, that same trajectory minimizing heat load minimizes the total integrated heat load as well, in addition to minimizing  $\Delta V$ .
- The introduction of the optimal aerocapture guidance with attitude kinematics constraints (OAK), an optimal NPC guidance for longitudinal aerocapture guidance that achieves optimal results with minimal tuning by constraining the attitude kinematics in the planning.
- The introduction of a lateral guidance that assumes immediate start of a bank reversal, allowing for almost single reversal lateral control.

This paper continues as follows. Section II describes the dynamics of aerocapture. Section III provides the analytical proof of the form of the trajectory that minimizes radiative heat. Section IV introduces both the longitudinal and the lateral logic of the novel guidance of this paper. Section V shows the results obtained from extensive simulation campaign. The guidance is tested for different entry conditions and vehicles. Section VI concludes this paper.

## II. The Aerocapture Maneuver

The dynamics of a vehicle undergoing aerocapture are dominated by gravitational and aerodynamic forces. Including the  $J_2$  component of the gravity field, the equations of motion of a vehicle in the atmosphere of a planet are [33]:

$$\dot{V} = -\frac{D}{m} - g_r \sin \gamma - g_\delta \cos \gamma \cos \chi + \omega_{cb}^2 r \cos \delta (\sin \gamma \cos \delta - \cos \gamma \sin \delta \cos \chi) \quad (1)$$

$$V\dot{\gamma} = \frac{L \cos \sigma}{m} - g_r \cos \gamma + g_\delta \sin \gamma \cos \chi + 2\omega_{cb} V \cos \delta \sin \chi + \frac{V^2}{r} \cos \gamma + \omega_{cb}^2 r \cos \delta (\cos \gamma \cos \delta - \sin \gamma \sin \delta \cos \chi) \quad (2)$$

$$V \cos \gamma \dot{\chi} = \frac{L \sin \sigma}{m} + g_\delta \sin \chi + 2\omega_{cb} V (\cos \gamma \sin \delta - \sin \gamma \cos \delta \cos \chi) + \frac{V^2}{r} \cos^2 \gamma \tan \delta \sin \chi + \omega_{cb}^2 r \cos \delta \sin \delta \sin \chi \quad (3)$$

$$\dot{r} = V \sin \gamma \quad (4)$$

$$\dot{\tau} = \frac{V \sin \chi \cos \gamma}{r \cos \delta} \quad (5)$$

$$\dot{\delta} = \frac{V \cos \gamma \cos \chi}{r} \quad (6)$$

where  $V$  is the relative velocity,  $\gamma$  is the relative flight-path angle,  $\chi$  is the relative heading angle,  $r$  is the radial distance from the center of the planet, and  $\tau$  and  $\delta$  are the longitude and latitude, respectively.  $L$  and  $D$  are the aerodynamic lift and drag,  $m$  is the vehicle mass,  $\omega_{cb}$  is the planet angular velocity, and  $\sigma$  is the bank angle.  $g_r$  and  $g_\delta$  are the two components of the gravity field, when the  $J_2$  zonal term is included:

$$g_\delta = -\frac{3}{2}\mu J_2 \frac{R_e^2}{r^4} \sin 2\delta \quad (7)$$

$$g_r = \mu \left[ -\frac{1}{r^2} + \frac{3}{2}J_2 \frac{R_e^2}{r^4} (3 \sin^2 \delta - 1) \right] \quad (8)$$

Standard coordinate transformations can link the above model to Keplerian orbits. Given a target circular orbit with semi-major axis  $a^*$ , and assuming an exit orbit with semi-major axis  $a$  and apoapsis  $r_a = a(1 + e)$ , the magnitude of planar  $\Delta V$ , required to raise the periapsis, as well as to correct the apoapsis, is [10]:

$$\Delta V = \|\Delta V_1\| + \|\Delta V_2\| = \sqrt{2\mu} \left( \left\| \sqrt{\frac{1}{r_a} - \frac{1}{r_a + a^*}} - \sqrt{\frac{1}{r_a} - \frac{1}{2a^*}} \right\| + \left\| \sqrt{\frac{1}{2a^*}} - \sqrt{\frac{1}{a^*} - \frac{1}{r_a - a^*}} \right\| \right) \quad (9)$$

This equation can easily be generalized to elliptical target orbits. However, this case will not be considered here, since circular target orbits benefit the most from aerocapture.

The  $\Delta V$  needed because of a change in inclination is:

$$\Delta V_i \approx 2V \sin\left(\frac{\Delta i}{2}\right) \quad (10)$$

Finally, the total  $\Delta V_{tot}$  that includes in-plane and out-of-plane components, is:

$$\Delta V_{tot} = \sqrt{\Delta V_1^2 + \Delta V_i^2} + \Delta V_2 \quad (11)$$

The out-of-plane correction is assumed here to be occurring entirely during the first burn. While the optimal strategy would be to leave a small portion of the correction for the second burn, the difference is negligible.

### III. Minimum Radiative Heat Aerocapture

It is possible to infer some analytical conclusions on the optimal aerocapture trajectory assuming that the central body is not rotating, and that there are no requirements on the final inclination nor final argument of periapsis. In such a case, an aerocapture leads to a minimum  $\Delta V_{tot}$  if the bank angle trajectory is full lift-up, followed by full lift-down [10].

Peak convective heat flux and structural load are too minimized by a bang-bang full lift-up, full lift-down trajectory [11]. Conversely, an aerocapture leads to minimum total convective heat if the bank angle history is full lift-down, full lift-up [12]. The two objectives thus lead to opposite trajectories. Nonetheless, during aerocapture a major source of heat flux comes from the radiation of incandescent gases in the shock-layer. For lunar return conditions on Earth, the total radiative heat load is comparable to the total convective heat load. For higher velocities, the ratio changes in favor of the radiative heat load. Thus, minimization of radiative heat load becomes much more important than minimization of the convective heat load for high speed aerocapture flown by large vehicles. The objective of this is section to prove that the integral of a class of monomial functions of density and velocity is minimized by a bang-bang trajectory. For many empirical formulations of the radiative heat flux[13, 34–37], such a trajectory is full lift-up, full lift-down, which corresponds to minimizing  $\Delta V_{tot}$ , the heat flux peak, and the dynamic pressure peak.

Let the heat flux be described as a generic function  $f = f(\rho, V)$ , where  $\rho = \rho_0 e^{-\beta h}$  is assumed to follow an exponential profile, and  $\beta$  is the inverse of the scale height. Neglecting requirements on the target orbit plane, for a spherical, non-rotating planet, Eqs. (1)-(6) reduce to:

$$\dot{V} = -\frac{D}{m} - \frac{\mu}{r^2} \sin \gamma \quad (12)$$

$$V\dot{\gamma} = \frac{L \cos \sigma}{m} - \frac{\mu}{r^2} \cos \gamma + \frac{V^2}{r} \cos \gamma \quad (13)$$

$$\dot{r} = V \sin \gamma \quad (14)$$

The cost function to be minimized is:

$$J = \int_{t_0}^{t_f} f(\rho, V) \quad (15)$$

Let us now assume that  $f(\rho, V)$  is separable, such that it can be decomposed as the product of a function of the density  $f_\rho(\rho)$  and a function of the velocity  $f_V(V)$ . For the special case where  $f_\rho(\rho) = \rho$  and  $f_V(V) = V^{n_V}$ , and assuming  $\dot{V} = D/m \gg g \sin \gamma$ , which is valid throughout the most relevant parts of the trajectory:

$$\int_0^{t_f} \rho V^{n_V} dt = \int_0^{t_f} \frac{\rho V^{n_V}}{\dot{V}} \frac{dV}{dt} dt = -m \int_{V_0}^{V_f} \frac{\rho V^{n_V}}{D} dV = -\frac{2m}{SC_d} \int_{V_0}^{V_f} V^{n_V-2} dV = \frac{2m}{(n_V-1)SC_d} \left( V_0^{n_V-1} - V_f^{n_V-1} \right). \quad (16)$$

The lift-up lift-down sequence provides the highest final velocity, and thus minimizes the cost integral as long as  $n_V > 1$ . However, the relative difference is negligible, especially for high  $n_V$ , where the initial velocity to the  $n_V^{\text{th}}$  power would dominate over any differences in the final velocity. This result can be generalized to any positive function  $f(\rho, V)$  of the form  $\rho f_V(V)$ , where the dependency on the velocity  $f_V(V)$  is an arbitrary function, as long as it can be separated from



$\rho$ :

$$\int_0^{t_f} \rho f_V(V) dt = -\frac{2m}{SC_d} \int_{V_0}^{V_f} \frac{f_V(V)}{V^2} dV = \frac{2m}{SC_d} (g(V_0) - g(V_f)), \quad (17)$$

where

$$g(V) = \int \frac{f_V(V)}{V^2} dV, \quad (18)$$

and only depends on the exit value of  $V$  which, again, has negligible dependency on the trajectory.

Let us now consider a more general case where  $f_\rho(\rho) = \rho^{m_\rho}$ . For a given trajectory, one has that the velocity continuously decreases as long as  $D/m > V \sin \gamma$ . Therefore, the density  $\rho(V)$  can be parameterized as a unique function of  $V$ . Neglecting the dependency of the final velocity  $V_f$  on the trajectory, which is small, the previous result shows that

$$\int_{t_0}^{t_f} \rho(V) f_V(V) dt = C, \quad \forall \rho(V), f_V(V), \quad (19)$$

where  $C$  is a constant independent of the flown trajectory. The following equality

$$\int_{t_0}^{t_f} \rho^{m_\rho}(V) f_V(V) dt = \int_{t_0}^{t_f} \left( \rho^{m_\rho-1}(V) \times (\rho(V) f_V(V)) \right) dt, \quad (20)$$

where the  $\times$  symbol has been used only to stress the separation in two factors, leads to realizing that the integral on the left side can be seen as the previous integral of Eq. (19), where each infinitesimal  $\rho(V) f_V(V) dt$  is multiplied by  $\rho^{m_\rho-1}$ .

Thus, if it exists, the optimal trajectory is such that

$$\rho_{opt}^{m_\rho-1}(V) < \rho^{m_\rho-1}(V) \quad \forall V. \quad (21)$$

For  $m_\rho > 1$ , that implies that the density has to be minimized, and therefore the altitude maximized, for every value of the velocity. Such trajectory is flown by first flying lift-up, then lift-down. For  $m_\rho < 1$  instead, the opposite trajectory should be flown. Note that for  $f_V(V) = V^3$  and  $m_\rho = 0.5$  one has the analytical equation for convective heat flux, hence this proof includes the minimum convective heat load proof of Ref. [12], and expands on it by offering an analytical proof for why the minimum convective heat trajectory has only one switch, starting with lift down. Additionally, this proof generalizes to other formulations of convective heat such as the Detra-Hidalgo [38], for which the exponent  $n_V$  is 3.15 instead of 3.

Let us generalize now the problem to any separable function  $f(\rho, V) = f_\rho(\rho) f_V(V)$ :

$$\int f_\rho(\rho(V)) f_V(V) dt = \int \rho^{-1}(V) (f_\rho(\rho(V)) f_V(V)) dt \quad (22)$$

**Table 1** Optimal control sequences as a function of  $f(\rho, V)$ .

properties of $f(\rho, V)$	properties of $f_\rho(\rho)$	optimal lift sequence
separable	$f_\rho(\rho)=\rho$	N/A
separable	$f_\rho(\rho)$ superlinear	up-down
separable	$f_\rho(\rho)$ sublinear	down-up
separable	$\rho^{-1}f_\rho(\rho)$ not monotonic	unresolved
not separable	N/A	unresolved

Now, the condition for optimality is:

$$\frac{f_\rho(\rho_{opt}(V))}{\rho_{opt}(V)} < \frac{f_\rho(\rho(V))}{\rho(V)} \quad \forall V. \quad (23)$$

If  $f_\rho(\rho)$  increases superlinearly for all  $\rho \in \mathbb{R}_+$ , the optimal trajectory is lift-up lift-down; if  $f_\rho(\rho)$  increases sublinearly or decreases for all  $\rho$ , the optimal trajectory is lift-down lift-up; if  $f_\rho(\rho)$  is linear the integral cost is independent of the trajectory. For all other cases, *e.g.*, when  $\rho^{-1}f_\rho(\rho)$  is not monotonic, no conclusion can be drawn based on this proof alone. Table 1 summarizes the results of this section. It is straightforward to expand the proof of this section to any functions of the form

$$f(\rho, V) = \sum_i f_{\rho,i}(\rho) f_{V,i}(V), \quad (24)$$

as long as  $f_{\rho,i}$  are all either superlinear or sublinear in  $\rho$ .

Many empirical radiative heat flux formulations can be separated between functions of density  $f_\rho(\rho)$  and function of velocity  $f_V(V)$ . Examples include the formulas by Martin [34], Tauber and Sutton[13], Brandis and Johnston [36], and more [35, 37, 39]. In all mentioned cases  $f_\rho(\rho)$  grows superlinearly\*, and the optimal trajectory is lift-up lift-down. As the formulation for convective heat is instead sublinear in  $\rho$ , this proof offers no insights on the trajectory minimizing the sum of convective and radiative heat. Fig. 3 shows the ratio between heat load flying a down-up sequence,  $Q_{d-u}$ , and heat load flying an up-down sequence,  $Q_{u-d}$ , as a function of entry flight path angle for various formulations of radiative heat flux, as well as for the convective heat flux. The trajectories all have initial velocities of 16 km/s and target an apoapsis of 500 km. The equations of motion used are the simplified set (12)-(14). Radiative heat according to any of the used formulations is lowest for up-down trajectories. At the same time, convective heat load is minimized by a down-up trajectories. The impact of the chosen trajectory on the radiative heat highly depends on the empirical formulation of choice, as well as the initial flight-path angle. Figure 4 shows the same ratio for entry flight path angle of  $-7^\circ$  for different monomial expressions of  $f(\rho, V) = c\rho^{m_\rho}V^{n_V}$  with varying exponents. Increasing  $m_\rho$  leads to favoring

\*The Tauber-Sutton formula is proportional to  $\rho^{1.22}R_n^a$ , where  $R_n$  is the nose radius and  $a \propto \rho^{-0.325}$ . It is therefore not straightforward to determine for which values it is monotonically increasing when  $R_n > 1$  m. However,  $a$  is capped between 0 and 1, and therefore non-monotonicity, if any, would be for a small interval. Similar claims can be made about Brandis-Johnston's formula. The formula of Ref. [37] includes a factor equal to  $\rho^{1.2-0.01223V}$ ,  $V$  in km/s, which is not separable; however, the dependency is very weak.

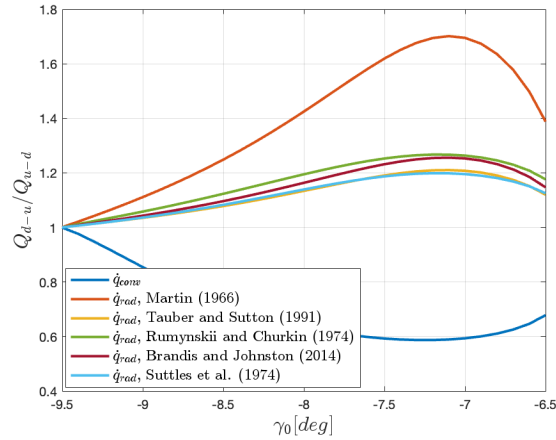


**Fig. 3 Heat ratio between down-up and up-down trajectories for different heat equations.**

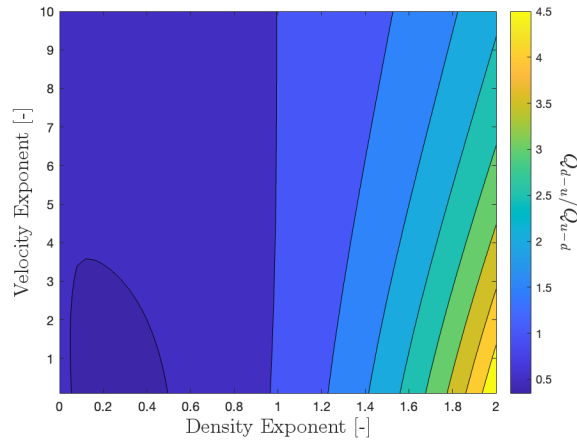


**Fig. 4 Heat ratio between down-up and up-down trajectories, varying exponents.**

the up-down trajectory more, as expected. On the other hand, higher  $n_V$  leads to reduced differences between the flown trajectories. The latter result makes intuitive sense: the higher the exponent on  $n_V$ , the more relevant the beginning of the trajectory is, when maneuverability is limited, and the difference between flown trajectories is small.

In conclusion, this section has proved that during aerocapture the integral of any separable function  $f_\rho(\rho)f_V(V)$ , where both  $f_\rho(\rho)$  and  $f_V(V)$  are positive and  $f_\rho(\rho)\rho^{-1}$  is monotonic, is minimized by a bang-bang trajectory with a single switch. The order of commands only depends on whether  $f_\rho(\rho)$  increases superlinearly, in which case the trajectory begins with lift up, or sublinearly, in which case the trajectory begins lift down.

#### IV. Optimal Aerocapture Guidance with Attitude-Kinematics Constraints

A bang-bang trajectory involves a long-lasting rotation, from the lift-up phase to the lift-down. Assuming a maximum angular rate of  $15^\circ/\text{s}$  and a maximum angular acceleration of  $5^\circ/\text{s}^2$ , a rotation of  $120^\circ$  would take around 11 s. As

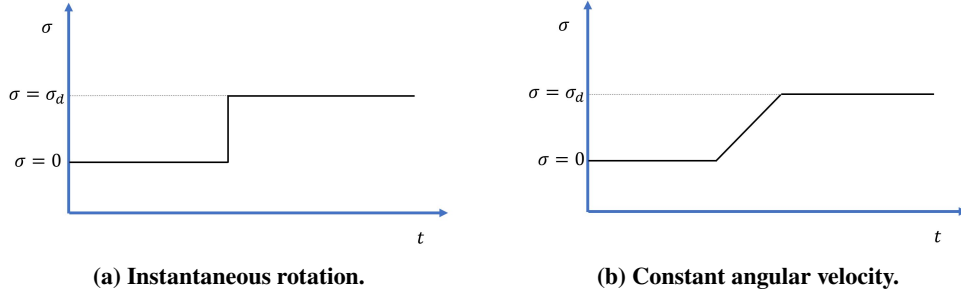


**Fig. 5 Options for bank angle planning during Phase 1.**

previously shown in Fig. 2, in such time more than 20% of the total energy difference may be depleted. An additional problem consists of the fact that the rotation occurs at very different moments of the trajectory, depending on the entry conditions. For a shallow entry, the rotation occurs very soon, when dynamic pressure is small, and thus the error in modeling does not impact the prediction much. For a steeper entry, the rotation would occur later, when the dynamic pressure is larger, causing larger errors. Consequently, we propose that a guidance logic include such a rotation in the trajectory planning. The rotation has been modeled in the guidance as occurring with infinite angular acceleration, but with an average angular rate of  $\dot{\sigma}_{exp} = 10.5^\circ\text{s}^{-1}$ , where the value is the average rotational speed assuming a rotation of  $120^\circ$  and accelerations and decelerations at  $5^\circ\text{s}^{-2}$ . This approximation can account for the majority of the error.

The rotational dynamics are less of an issue when having a bank inversion. In fact, independently of the angle at which the inversion starts, the inversion will end with an angle that is closer to  $90^\circ$  than the initial one. This leads to a small decrease in performance, but an increase in robustness at the same time.

This section introduces the Optimal aerocapture guidance with Attitude-Kinematics constraints (OAK), which expands on the FNPAG [10] by including a simplified model for the rotation of the vehicle. Similarly to FNPAG, the trajectory is divided into two phases.

### A. Longitudinal Guidance

During Phase 1, the algorithm integrates the equations of motion using a bank angle profile that varies linearly with rate  $\dot{\sigma}_{exp}$  from the current bank angle to  $\sigma_d$ , and then remains constant.  $\sigma_d$  is the bank angle value planned during Phase 1 to be used in Phase 2. If the so-predicted apoapsis is lower than the desired apoapsis, then the command does not change. Else, the command becomes equal to  $\sigma_d$ , and Phase 2 is triggered starting from the next guidance call. This causes a delay in the beginning of Phase 2 of no more than one sample time. Nonetheless, this phase requires only one iteration per guidance call, and the frequency can be increased, reducing the delay. Figure 5 shows the difference between the planning of Phase 1 as in Refs [10, 25], which assumes infinite angular velocity, and the planning in the current work. During Phase 2, the logic iterates to find a constant bank angle that leads to the desired apoapsis. Given the strong discontinuities, bisection is used, which leads to an accuracy of  $0.05^\circ$  after 13 iterations.

Density filters are implemented as in Ref. [10]. In the inner loop, the modeled lift and drag are multiplied by the scale factors  $\tilde{\rho}_L$ , and  $\tilde{\rho}_D$ , respectively. Given  $\rho_L$ ,

$$\rho_L = L/L^* \quad (25)$$

where  $L$  is the sensed lift, and  $L^*$  is the lift according to the model, the corresponding scale factor  $\tilde{\rho}_L$  is updated at each cycle, applying a low-pass filter:

$$\tilde{\rho}_L^{(n+1)} = \tilde{\rho}_L^{(n)} + (1 - k) (\rho_L - \tilde{\rho}_L^{(n)}) \quad (26)$$

The same applies to  $\tilde{\rho}_D$ . In this work, a value of  $k = 0.95$  has been used.

## B. Lateral logic

The lateral logic is specific for this guidance scheme. The guidance is designed to target the final inclination with high accuracy and with at most two reversals. Limiting the number of reversals reduces the impact of the lateral guidance on the longitudinal performance.

During Phase 1, the bank angle is kept constant. Once Phase 2 begins, the initial sign of the bank angle is chosen such that the inclination error is reduced. In this phase, the planning assumes that a bank reversal is initiated immediately, and it is simulated with the same rotational constraints described in the previous section.

Let  $\Delta i_{rev}$  be the approximate change in inclination that occurs during the bank reversal:

$$\Delta i_{rev} = \|i_{rev} - i\| \quad (27)$$

where  $i_{rev}$  is the predicted final inclination at time  $t_{rev} = 2 \min(\pi - \sigma, \sigma) / \dot{\sigma}_{exp}$ , and  $i$  is the instantaneous inclination at the initiation of the current guidance call. A bank inversion is triggered when all of the following conditions are true:

- 1) the inclination error at the end of the predicted trajectory,  $\Delta i_{pred}$ , and the current inclination error,  $\Delta i$ , have opposite signs:  $\Delta i_{pred} \times \Delta i < 0$
- 2)  $\Delta i_{pred}$  is smaller than  $i_m$  times the current inclination error  $\Delta i$  plus  $\Delta i_{rev}/2$ :  $\Delta i_{pred} < i_m (\Delta i + \Delta i_{rev}/2)$ , and
- 3)  $\Delta i_{pred}$  is larger than a maximum allowable inclination error threshold  $\Delta i_t$ :  $\|\Delta i_{pred}\| > \Delta i_t$ .

By doing so, and by setting a margin  $i_m$ , the number of reversals can be limited to two. Too small a margin may lead to large final errors in the inclination, whereas a too large margin would lead to additional reversals. Since the latter situation is less problematic, when in doubt a larger margin should be preferred to an excessively small one. If a maximum number of reversals is set,  $i_m$  is automatically set to 0 before the last reversal. Note that the bank reversal only occurs if the conditions for the reversal are met. This leads to a small, constant deviation in the longitudinal guidance; on the other hand, this allows much more accurate prediction if the reversal happens.

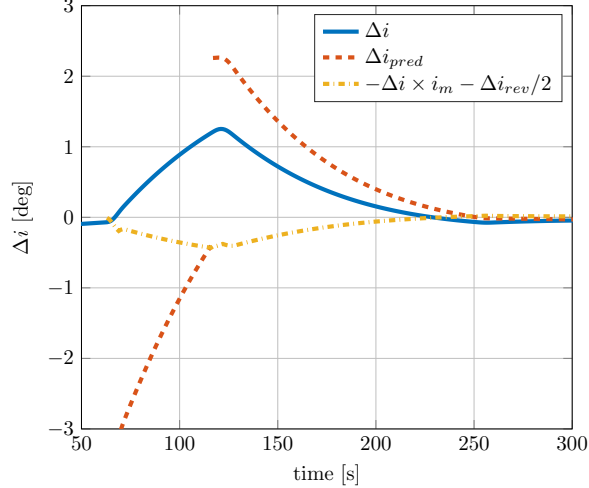


**Fig. 6 Schematic of the lateral logic during Phase 2;  $i_m = 0.3$ .**

A schematic of the lateral guidance is given in Fig. 6. Once the predicted inclination (dashed line) becomes smaller in absolute sense than the sum of current inclination (multiplied by  $i_m$ ) and  $\Delta i_{rev}/2$  (dashdotted line), the reversal begins. The margin  $i_m$  is needed because of the many perturbations that may happen after the reversal. In this paper, a 2-reversal strategy with  $i_m = 0.3$  is used.

## V. Experiments

Testing was carried out using a simulator for atmospheric flight on Earth, that was built, verified, and validated. The simulator includes Earth GRAM large-scale<sup>†</sup> density perturbations [40], a second-order gravity model, and Orion and Apollo databases. The database for Orion is for trim conditions at hypersonic flight, and uncertainties in aerodynamic coefficients as in Ref. [41]. Apollo is modeled in trim conditions as in Ref. [42]; uncertainties of aerodynamic coefficients are uniform for Apollo, in a range of  $\pm 20\%$ . A bank angle deadband of  $0.1^\circ$  has been implemented for both vehicles. Initial conditions are as given in Ref. [10]. The target orbit has an apoapsis altitude of 200 km, and an inclination of  $90^\circ$ . The guidance is triggered once a non-gravitational acceleration larger than 0.05 g is sensed. It is shut down when the spacecraft crosses 100 km altitude. The simulation is stopped once apoapsis is reached. For all simulations, a maximum of two reversals has been chosen, together with an initial margin of 30%.

### A. Concept comparison

The behavior of the guidance is evaluated in single, ideal cases; the comparison is done with respect to Mode 1 of the optimal aerocapture guidance<sup>‡</sup> by Lu et al. [10]. The guidance is then compared in Monte Carlo simulations along a wide range of entry angles and perturbations. The comparison is against FNPAG, and Mode 6 of PredGuid+A [43].

<sup>†</sup>The baseline atmosphere used is instead the U.S. Standard Atmosphere of 1976.

<sup>‡</sup>The guidance logic is not exactly the same, mainly because the lateral logic proposed in this paper has been used.

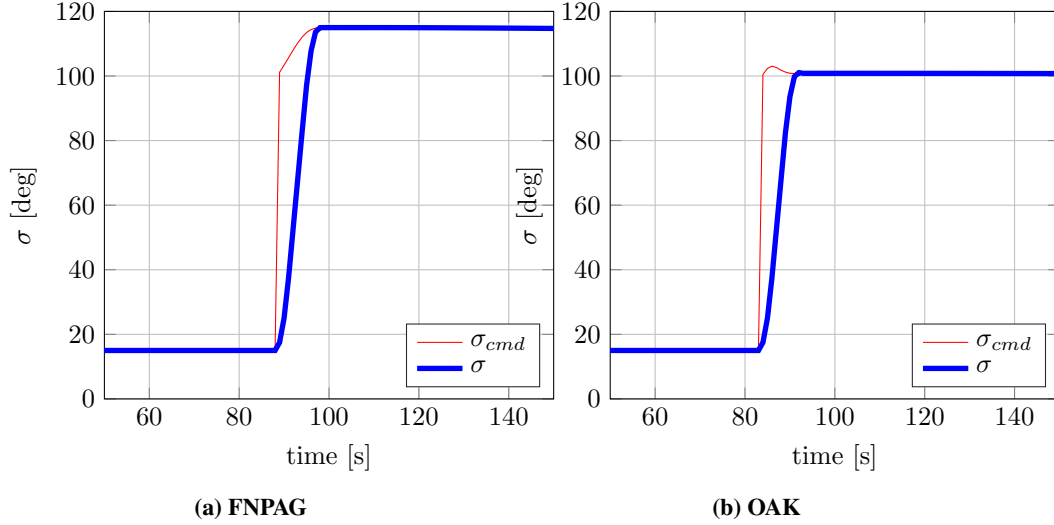


**Fig. 7 Bank angle history during flight in ideal conditions,  $\sigma_d = 100^\circ$ .**

PredGuid+A Mode 6 is a numerical predictor-corrector in which a constant bank angle is chosen at every iteration, such that the predicted apoapsis is equal to the target. Since FNPAG requires an intensive interpolation that depends on the vehicle, the central body, and the entry conditions, such a comparison has to be carried out using Orion as reference vehicle. Given the different perturbation settings, it may be that the optimal tuning for this case will be slightly different from the one of the original work. The tuning is obtained from interpolation of the data in Fig. 10 of Ref. [10]. Figure 7 shows the bank angle history under ideal conditions, with the FNPAG and the OAK guidance, respectively. The planned bank angle  $\sigma_d$  for Phase 2 is set to  $100^\circ$ . Here, the environment is modeled exactly the same as in the guidance logic. The bank angle is optimally controlled (according to a minimum-time problem), constrained by maximum angular acceleration and velocity, and is not subjected to any perturbations. Even for such ideal conditions, with FNPAG the duration of the rotation is long enough to cause a major shift of the final bank angle. Moreover, such a shift depends on the initial entry angle: an aerocapture with shallower entry angle lasts longer and is subjected to a smaller maximum dynamic pressure than an aerocapture with a steeper entry angle would be. Consequently, the effect of the bank angle rotation is less pronounced in the former case. This reasoning is in agreement with the optimal tuning obtained by Ref. [10]: in fact, the planned  $\sigma_d$  is larger for shallower entries, where the error caused is smaller; a larger margin is instead required for steeper entries.

## B. Simulation Results

The second part of the results is a Monte Carlo campaign. The comparison is between the tuned FNPAG and the OAK guidance with  $\sigma_d = 120^\circ$ . Figure 8a shows that, in terms of apoapsis accuracy, the two concepts are rather similar. Similarly, Fig. 8b shows that the OAK guidance achieves comparable  $\Delta V$  for shallow entry angles. As expected, the performance of the longitudinal guidance is rather similar between OAK and FNPAG. The main difference consists of

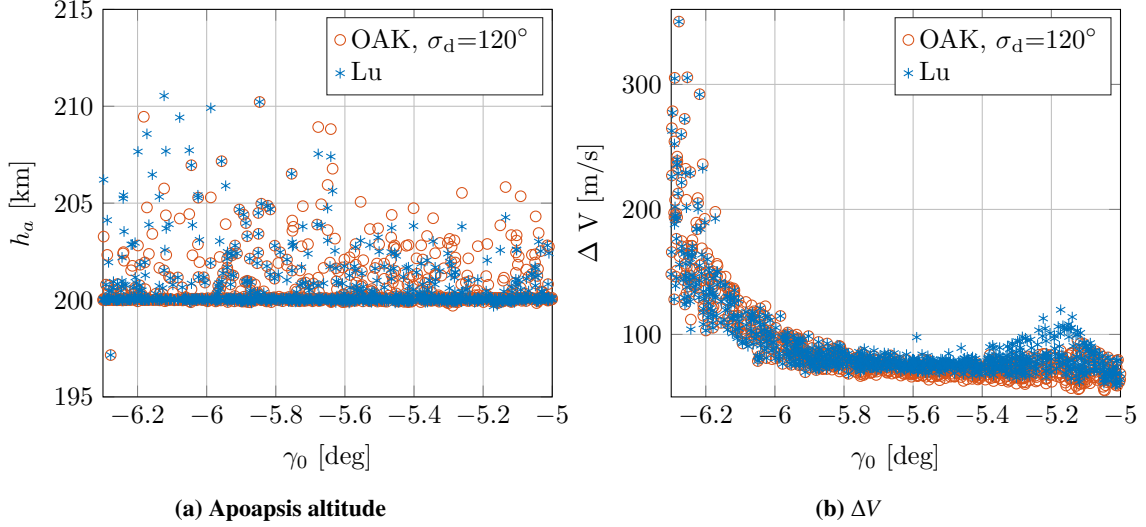


**Fig. 8 Comparison between FNPAG and OAK,  $\sigma_d = 120^\circ$ .**

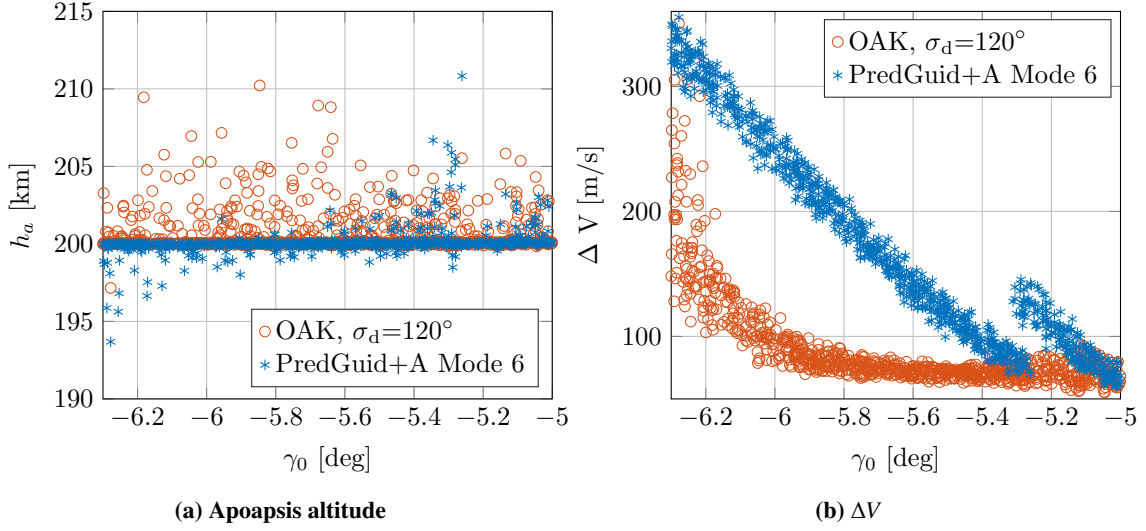
the fact that the FNPAG guidance requires extensive tuning, where a value of  $\sigma_d$  has to be found via Monte Carlo trials for each combination of entry velocity and angle. On the other hand, the OAK guidance can be set by defining a single parameter. In addition, the OAK guidance is conceptually more robust, as demonstrated in the previous subsection.

Figure 9 compares the performance of the OAK guidance against PredGuid+A, Mode 6 [43] (which is equivalent to OAK, with  $\sigma_d = 0^\circ$ ). While the OAK guidance is more accurate in terms of apoapsis targeting, the difference is not large. On the other hand the OAK guidance performs much better in terms of propellant usage, as expected. For entry angles around  $-5.8^\circ$ , the  $\Delta V$  needed using PredGuid+A Mode 6 is around 200 m/s, approximately 2.5 times more than what is obtained with OAK for the same conditions. The rightmost branch of the  $\Delta V$  with PredGuid+A Mode 6 is a strict consequence of the lateral logic. In fact, for the range of entry angles between  $-6.3^\circ$  and  $-5.3^\circ$ , the first bank reversal occurs when the commanded bank angle is smaller than  $90^\circ$ . As a consequence, the first rotation is upwards (thanks to the proposed lateral logic being used, rotations after the first one have almost negligible effect on the longitudinal performance). This causes an increase in performance, for the same reason why a full lift-up, full lift-down trajectory is the optimal one. For shallower entry angles, the opposite happens, causing a decrease in performance. Such pattern does not occur with the OAK guidance. As long as  $\sigma_d \geq 105^\circ$ , the rotation is always downwards. Nonetheless, the rotation is also shorter, and affects the performance less.

### C. Sensitivity with respect to $\sigma_d$

This subsection analyzes how a change in  $\sigma_d$  affects the performance of the guidance over the full range of entry conditions. Figure 10 shows apoapsis altitude and planar  $\Delta V$  for the OAK guidance with three values of  $\sigma_d$ :  $105^\circ$ ,  $120^\circ$ , and  $135^\circ$ . While  $\sigma_d = 135^\circ$  performs best in terms of planar  $\Delta V$ , it also causes the largest errors in apoapsis altitude (there is one outlier that is not shown in the figure, for  $\sigma_d = 135^\circ$ , with  $\gamma_0 = -5.045^\circ$ , and apoapsis altitude 268.7 km).





**Fig. 9 Comparison between PredGuid+A Mode 6 and OAK,  $\sigma_d = 120^\circ$ .**

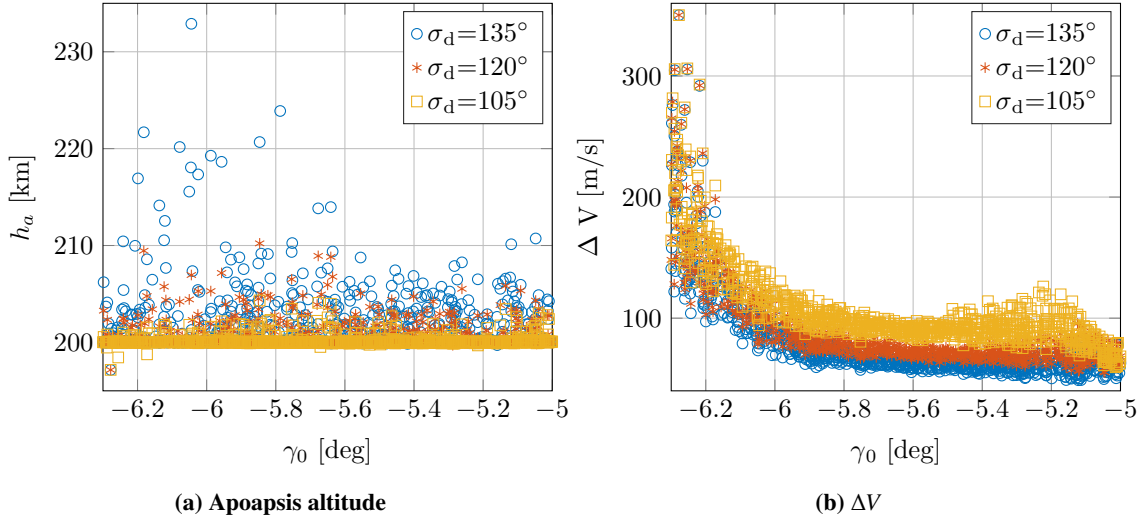


**Fig. 10 Comparison between different values of  $\sigma_d$  for the OAK guidance.**

These cases are caused by early saturation of the command. Saturation does not generally cause a sensible increase in planar  $\Delta V$ , but prevents lateral control. This, in turn, causes large inclination errors that imply large out-of-plane corrections.

As a consequence, robustness should therefore be evaluated in terms of  $\Delta V_{tot}$ , which is the  $\Delta V$  required to correct orbit shape and plane at the same time. The maximum value of this parameter is an important spacecraft design parameter. The analysis is limited for entry angles between  $-6^\circ$  and  $-5^\circ$ . In this range, the optimal  $\Delta V$  is approximately constant. Tables 2 and 3 summarize the main performance parameters for the OAK guidance with different values of  $\sigma_d$ . On average,  $\sigma_d = 135^\circ$  provides the best results, both for in-plane and total  $\Delta V$ . Nonetheless, such setting causes a few cases in which the final inclination error is very large, as mentioned before. Saturation happens also for lower values of

**Table 2 Summary of OAK guidance systems longitudinal performances, for  $\gamma_0 \in (-6^\circ, -5^\circ)$ .**

$\sigma_d$ [deg]	In-plane $\Delta V$ [m/s]				$\ \Delta r_{apo}\ $ [km]	$\Delta r_{apo}$ [km]			
	Mean	Min	Max	Std	Mean	Mean	Min	Max	Std
105	92.13	59.47	130.46	11.10	0.252	0.223	-0.476	4.328	0.590
120	74.21	55.19	114.74	49.1	0.698	0.677	-0.295	10.221	1.339
135	64.0	48.8	100.1	7.5	1.64	1.63	-0.28	68.73	3.70

**Table 3 Summary of OAK guidance systems lateral performances, for  $\gamma_0 \in (-6^\circ, -5^\circ)$ .**

$\sigma_d$ [deg]	$\ \Delta i\ $ [°]	$\Delta i$ [°]				$\Delta V_{tot}$ [m/s]			
	Mean	Mean	Min	Max	Std	Mean	Min	Max	Std
105	0.038	-0.023	-0.081	0.082	0.033	92.29	59.98	130.61	11.05
120	0.036	-0.023	-0.096	0.111	0.034	74.41	55.35	114.77	8.12
135	0.034	-0.018	-0.818	0.207	0.050	64.41	49.13	137.25	7.93

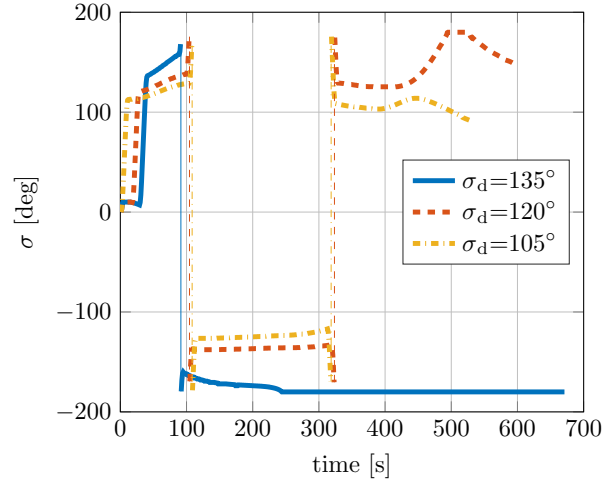


**Fig. 11 Bank angle history for OAK guidance with different values of  $\sigma_d$ , in a case of strong perturbations.**

$\sigma_d$ , but later and with much smaller effect in the final inclination error. Figure 11 shows the bank angle history of the three guidance logics for same conditions and perturbations. Where the one with highest  $\sigma_d$  saturates rapidly, leading to a final inclination error of more than  $0.8^\circ$ , the remaining two do not, leading to inclination errors of only  $0.03^\circ$  ( $\sigma_d = 120^\circ$ ) and  $0.01^\circ$  ( $\sigma_d = 105^\circ$ ).

#### D. Vehicle sensitivity

This subsection analyzes whether the same parameter tuning can work on different vehicles. The performance of this guidance is analyzed using Apollo instead of Orion as a reference vehicle. Apollo has a 20% larger lift-to-drag ratio and a 7% smaller ballistic coefficient. Further, the uncertainties in the aerodynamic coefficients have been increased:  $C_D$  and  $C_L$  now both vary between  $\pm 20\%$ , and independently from each other. Figure 12 shows the apoapsis altitude

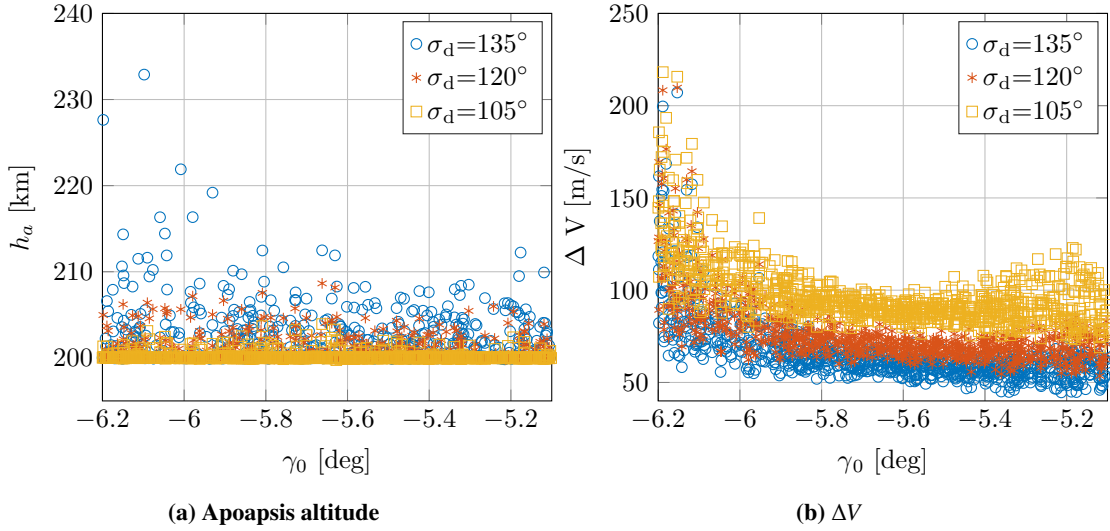


**Fig. 12 Comparison between different values of  $\sigma_d$  for the OAK guidance.**

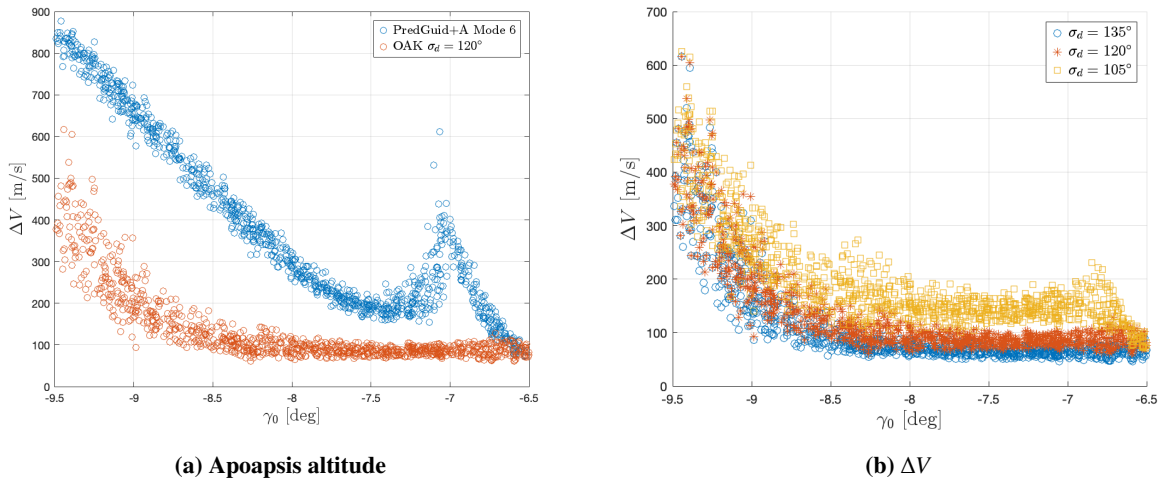


**Fig. 13 Comparison between PredGuid+A Mode 6 and different values of  $\sigma_d$  for the OAK guidance.**

and planar  $\Delta V$  for Apollo, in a slightly different range of initial flight-path angles to reflect the difference in aerocapture corridor. The figure shows a pattern very similar to the one of Orion. The worst case of  $\Delta V_{tot}$  is best for  $\sigma_d = 120^\circ$ , and equal to 96.7 m/s; the worst case with  $\sigma_d = 135^\circ$  is 106.8 m/s instead. Hence, the best  $\sigma_d$  is approximately the same for both tested vehicles.

### E. High-Speed Aerocapture

This subsection shows results for higher speed aerocapture, with an entry velocity of 16 km/s. The entry corridor is adjusted accordingly, with  $\gamma_0 \in [-9.5^\circ, -6.5^\circ]$ . Results are only compared with PredGuid+A Mode 6, since FNPAG would require new extensive tuning for these entry conditions. Figure 13 reports performance in terms of planar

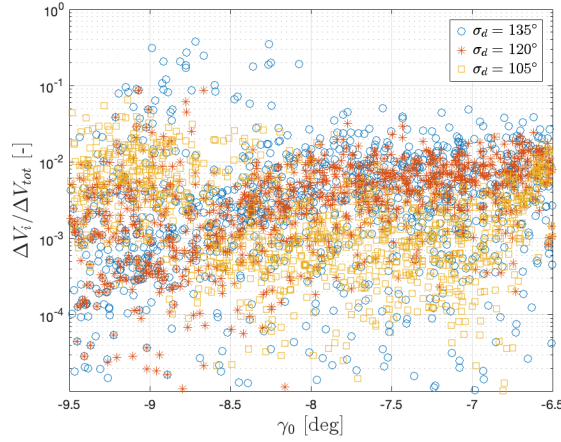


**Fig. 14 Lateral logic performance.**

$\Delta V$ . For every conditions under consideration, the OAK guidance consistently outperforms PredGuid+A Mode , as expected. The results demonstrate again that the OAK guidance is easy to tune, since the same parameters for lunar return conditions give comparable results for higher speed aerocapture. Similarly to the slower aerocapture, there is a wide range of entry conditions where the OAK guidance can consistently provide a  $\Delta V$  independently of initial flight path angle. The average of in-plane  $\Delta V$  decreases with increasing  $\sigma_d$  up to  $135^\circ$ . The optimal value of  $\sigma_d$  is  $120^\circ$  when considering out-of-plane corrections too, both in terms of worst case scenarios and average.

### F. Lateral Logic Performance

The performance of the lateral guidance is evaluated for the high-speed aerocapture, with  $V_0 = 16$  km/s. The performance metric is the ratio between  $\Delta V_i$  needed to enter the right inclination, and the total  $\Delta V_{tot}$ , which includes periapsis raise, inclination correction, and apoapsis correction. Fig. 14 shows the results as a function of initial flight path angle and  $\sigma_d$ . As implied from previous results, the guidance  $\sigma_d = 135^\circ$  induces unreliability in the lateral logic. The only cases where the inclination change accounts for more than 10% occur with that setting. Moreover, steep entry angles are generally the cause for more inclination errors, which is to be expected because maneuverability is limited due keeping a bank angle very close to zero for a large portion of the trajectory.

### G. Heat load

This subsection validates the proof of Sec. III in a less simplified environment. For convective and radiative heat, a nose radius of 6.03 m has been used. Convective, radiative (with Tauber-Sutton), and total heat loads are shown in Fig. 15 for all the lunar return trajectories guided by the OAK guidance with  $\sigma_d = 120^\circ$ . For steep entries radiative heat load is larger than the convective one; the opposite is true for shallow entry angles, which are closer to the case that maximizes convective heat load. Radiative heat load decreases mildly for shallow entry angles. For larger entry

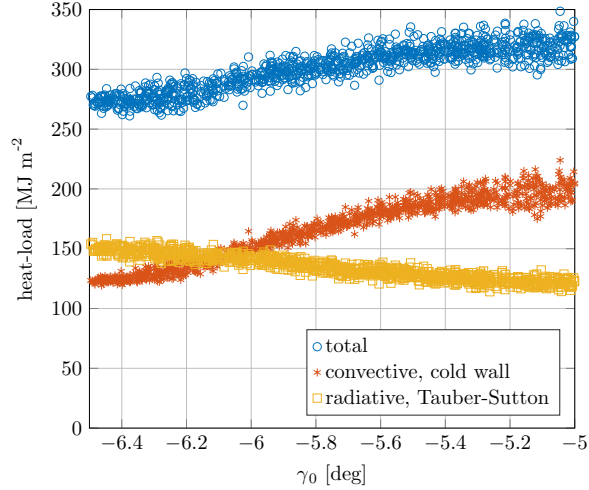


**Fig. 15** heat loads for dispersed conditions using the OAK guidance,  $\sigma_d = 120^\circ$ , lunar return conditions.

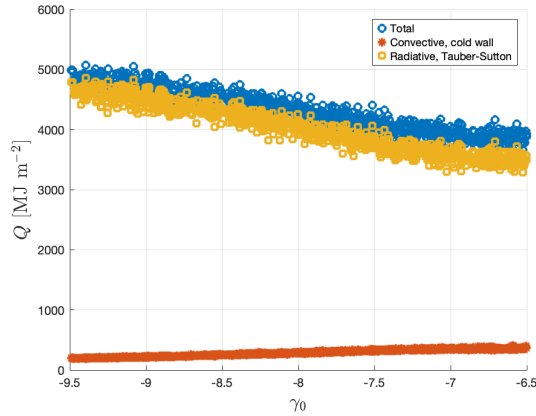


**Fig. 16** heat loads for dispersed conditions using the OAK guidance,  $\sigma_d = 120^\circ$ ,  $V_0 = 16$  km/s.

velocities, reported in Fig. 16, radiation become even more relevant. For entry at 16 km/s, convective heat becomes negligible. Note that the ratio between the two heat sources is strongly dependent not only on entry conditions, but also on the vehicle itself: while the convective heat load is decreasing  $R_n$ , the radiative heat load is increasing. Thus, for larger vehicles convection can be neglected entirely.

Figure 17 shows the ratio of different formulations of components of the heat loads between same trajectories flown with OAK guidance and PredGuid+A Mode 6. This figure is a numerical validation of Fig. 3. Note that the ratios are less pronounced here, for two main reasons: 1) the OAK guidance does not follow an exact bang-bang trajectory because of the set margin, as well as because of perturbations; and 2) the comparison is against a guidance that flies at constant bank angle, instead of flying lift down followed by lift up. As the convective heat is much smaller in high-speed environments, a reduction by 5 to 10% in radiative heat is more impactful on the total than a reduction by 20% in convective heat. While an up-down trajectory provides less heat than a down-up trajectory for aerocapture. This is

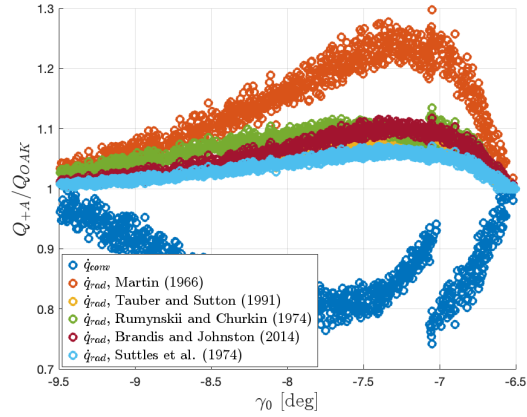


**Fig. 17** Ratio between heat with OAK guidance and heat with PredGuid+A Mode 6.

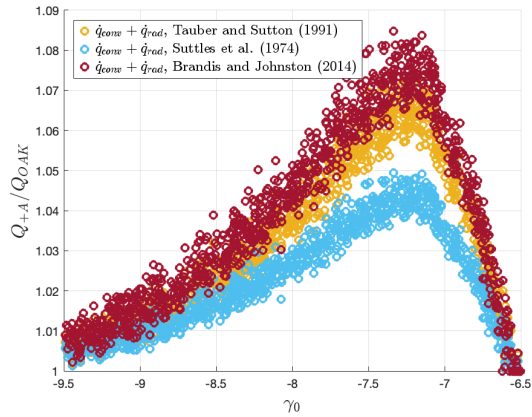


**Fig. 18** Ratio between heat with OAK guidance and heat with PredGuid+A Mode 6.

further demonstrated by Fig. 18, which shows the ratio between the two guidance logics for the sums of convective and radiative heats. Independent of the used formulations, OAK outperforms the baseline, albeit only between 4 and 9%. Some formulations of radiative heat flux have not been used for these results because of the challenges in recovering the proportionality constants.

## VI. Conclusions

This paper brings three major contributions. First, it is analytically proven that, for several analytical approximations of the radiative heat flux, the aerocapture trajectory minimizing the  $\Delta V$  also minimizes the radiative heat load. The results are validated numerically. As radiative heat load grows rapidly with increasing velocity, its minimization is especially relevant for high-speed missions. Further, as radiative heat grows with the nose radius, whereas convective heat decreases, effect of radiation is more relevant for larger spacecraft. Interestingly, the minimum radiative heat trajectory coincides with the trajectory that minimizes also  $\Delta V$ , peak heat flux, and peak aerodynamic load. Hence, for

missions where radiative heat load is much larger than convective heat load, there is no need to seek trade-offs between costs. Radiative heat load can be reduced by a factor between 15 and 60% when flying an optimal trajectory. The second contribution is the introduction of a new longitudinal guidance, which takes attitude constraints into account. This guidance achieves similar optimal performance as the algorithms from Refs. [10] or [25], but it does so with much less tuning. The tuning of the longitudinal guidance is robust to wide differences in initial flight path angle and velocity, as well as for two different vehicles. Third, a novel lateral guidance is introduced. The lateral guidance is robust and generally only requires one or two reversals. Few reversals lead to less interference with the longitudinal planning. For lunar return conditions this lateral guidance guarantees a maximum inclination error of  $0.082^\circ$ , and the corresponding correction never exceeds 4 m/s. For high-speed aerocapture, the lateral correction is limited to less than 10% of the total  $\Delta V$ .

### Acknowledgments

Research was done at Delft University of Technology, in the Astrodynamics and Space Missions Section, when Enrico M. Zucchelli was an M.Sc. Graduate student.

### References

- [1] Cruz, M. I., “The aerocapture vehicle mission design concept,” *Conference on Advanced Technology for Future Space Systems*, Hampton, VA, 1979. <https://doi.org/10.2514/6.1979-893>.
- [2] Hall, J. L., Noca, M. A., and Bailey, R. W., “Cost-Benefit Analysis of the Aerocapture Mission Set,” *Journal of Spacecraft and Rockets*, Vol. 42, No. 2, 2005, pp. 309–320. <https://doi.org/10.2514/1.4118>.
- [3] Munk, M. M., and Moon, S. A., “Aerocapture Technology Development Overview,” *2008 IEEE Aerospace Conference*, 2008, pp. 1–7. <https://doi.org/10.1109/AERO.2008.4526545>.
- [4] Spilker, T. R., Adler, M., Arora, N., Beauchamp, P. M., Cutts, J. A., Munk, M. M., Powell, R. W., Braun, R. D., and Wercinski, P. F., “Qualitative Assessment of Aerocapture and Applications to Future Missions,” *Journal of Spacecraft and Rockets*, Vol. 56, No. 2, 2019, pp. 536–545. <https://doi.org/10.2514/1.A34056>.
- [5] Girija, A. P., Saikia, S. J., Longuski, J. M., Lu, Y., and Cutts, J. A., “Quantitative Assessment of Aerocapture and Applications to Future Solar System Exploration,” *Journal of Spacecraft and Rockets*, Vol. 59, No. 4, 2022, pp. 1074–1095. <https://doi.org/10.2514/1.A35214>.
- [6] Saikia, S. J., Millane, J., Lu, Y., Mudek, A., Arora, A., Witsberge, P., Hughes, K., Longuski, J. M., Spilker, T., Petropoulos, A., Arora, N., Cutts, J., Elliott, J., Sims, J., and Reh, K., “Aerocapture Assessment for NASA Ice Giants Pre-Decadal Survey Mission Study,” *Journal of Spacecraft and Rockets*, Vol. 58, No. 2, 2021, pp. 505–515. <https://doi.org/10.2514/1.A34703>.

- [7] Girija, A. P., Saikia, S. J., Longuski, J. M., Bhaskaran, S., Smith, M. S., and Cutts, J. A., “Feasibility and Performance Analysis of Neptune Aerocapture Using Heritage Blunt-Body Aeroshells,” *Journal of Spacecraft and Rockets*, Vol. 57, No. 6, 2020, pp. 1186–1203. <https://doi.org/10.2514/1.A34719>.
- [8] Deshmukh, R. G., Spencer, D. A., and Dutta, S., “Investigation of direct force control for aerocapture at Neptune,” *Acta Astronautica*, Vol. 175, 2020, pp. 375–386. <https://doi.org/https://doi.org/10.1016/j.actaastro.2020.05.047>.
- [9] Miele, A., Wang, T., Lee, W., and Zhao, Z., “Optimal trajectories for the aeroassisted flight experiment,” *Acta Astronautica*, Vol. 21, No. 11, 1990, pp. 735–747. [https://doi.org/10.1016/0094-5765\(90\)90116-3](https://doi.org/10.1016/0094-5765(90)90116-3).
- [10] Lu, P., Cerimele, J., Tigges, M., and Matz, D., “Optimal Aerocapture Guidance,” *Journal of Guidance, Control, and Dynamics*, Vol. 38, No. 4, 2015, pp. 553–565.
- [11] Miele, A., and Wang, T., “General solution for the optimal trajectory of an AFE-type spacecraft,” *Acta Astronautica*, Vol. 26, No. 12, 1992, pp. 855–866. [https://doi.org/10.1016/0094-5765\(92\)90125-3](https://doi.org/10.1016/0094-5765(92)90125-3).
- [12] Sigal, E., and Guelman, M., “Aerocapture with minimum total heat,” *Proceedings of the 52nd International Astronautical Congress*, Toulouse, France, 2001.
- [13] Tauber, M. E., and Sutton, K., “Stagnation-point radiative heating relations for Earth and Mars entries,” *Journal of Spacecraft and Rockets*, Vol. 28, No. 1, 1991, pp. 40–42. <https://doi.org/10.2514/3.26206>.
- [14] Brykina, I. G., and Egorova, L. A., “Approximation formulas for the radiative heat flux at high velocities,” *Fluid Dynamics*, Vol. 54, 2019, pp. 562–574. <https://doi.org/10.1134/S0015462819040037>.
- [15] Morgan, J., Williams, J., Venkataphy, E., Gasch, M., Deshmukh, R., Shellabarger, E., Scoggins, J. B., Gomez-Delrio, A. J., Tackett, B., and Dutta, S., “Thermal Protection System Design of Aerocapture Systems for Uranus Orbiters,” *AIAA SCITECH 2024 Forum*, Orlando, FL, 2024. <https://doi.org/10.2514/6.2024-0952>.
- [16] Grinstead, J. H., Wright, M. J., Bogdanoff, D. W., and Allen, G. A., “Shock Radiation Measurements for Mars Aerocapture Radiative Heating Analysis,” *Journal of Thermophysics and Heat Transfer*, Vol. 23, No. 2, 2009, pp. 249–255. <https://doi.org/10.2514/1.37281>.
- [17] Olejniczak, J., Prabhu, D., Wright, M., Takashima, N., Hollis, B., Sutton, K., and Zoby, E., “An analysis of the radiative heating environment for aerocapture at Titan,” *39th AIAA/ASME/SAE/ASEE Joint Propulsion Conference and Exhibit*, 2003, p. 4953. <https://doi.org/10.2514/6.2003-4953>.
- [18] Hollis, B., Wright, M., Olejniczak, J., Takashima, N., Sutton, K., and Prabhu, D., “Preliminary Convective-Radiative Heating Environments for a Neptune Aerocapture Mission,” *AIAA Atmospheric Flight Mechanics Conference and Exhibit*, Providence, RI, 2004. <https://doi.org/10.2514/6.2004-5177>.
- [19] Brandis, A. M., and Cruden, B. A., “Titan Atmospheric Entry Radiative Heating,” *47th AIAA Thermophysics Conference*, Denver, CO, 2017. <https://doi.org/10.2514/6.2017-4534>.



- [20] McEneaney, W. M., "Optimal aeroassisted guidance using Loh's term approximations," *Journal of Guidance, Control, and Dynamics*, Vol. 14, No. 2, 1991, pp. 368–376. <https://doi.org/10.2514/3.20648>.
- [21] Calise, A. J., and Melamed, N., "Optimal guidance of aeroassisted transfer vehicles based on matched asymptotic expansions," *Journal of Guidance, Control, and Dynamics*, Vol. 18, No. 4, 1995, pp. 709–717. <https://doi.org/10.2514/3.21451>.
- [22] Melamed, N., and Calise, A. J., "Evaluation of optimal-guidance algorithm for aeroassisted orbit transfer," *Journal of Guidance, Control, and Dynamics*, Vol. 18, No. 4, 1995, pp. 718–722. <https://doi.org/10.2514/3.21452>.
- [23] Gurley, J. G., "Guidance for an aerocapture maneuver," *Journal of Guidance, Control, and Dynamics*, Vol. 16, No. 3, 1993, pp. 505–510. <https://doi.org/10.2514/3.21038>.
- [24] Powell, R. W., and Braun, R. D., "Six-degree-of-freedom guidance and control analysis of Mars aerocapture," *Journal of Guidance, Control, and Dynamics*, Vol. 16, No. 6, 1993, pp. 1038–1044. <https://doi.org/10.2514/3.21125>.
- [25] Evans, S. W., and Dukeman, G. A., "Examination of a practical aerobraking guidance algorithm," *Journal of Guidance, Control, and Dynamics*, Vol. 18, No. 3, 1995, pp. 471–477. <https://doi.org/10.2514/3.21411>.
- [26] Heidrich, C. R., Holzinger, M. J., and Braun, R. D., "Optimal Information Filtering for Robust Aerocapture Trajectory Generation and Guidance," *Journal of Spacecraft and Rockets*, Vol. 59, No. 2, 2022, pp. 524–537. <https://doi.org/10.2514/1.A35175>.
- [27] Ridderhof, J., and Tsiotras, P., "Stochastic Atmosphere Modeling for Risk Adverse Aerocapture Guidance," *2020 IEEE Aerospace Conference*, 2020, pp. 1–7. <https://doi.org/10.1109/AERO47225.2020.9172724>.
- [28] Zucchelli, E. M., Hanasusanto, G. A., Jones, B. A., and Mooij, E., "Two Stage Optimization for Aerocapture Guidance," *AIAA Scitech 2021 Forum*, 2021. <https://doi.org/10.2514/6.2021-1569>.
- [29] Masciarelli, J., Rousseau, S., Fraysse, H., and Perot, E., "An analytic aerocapture guidance algorithm for the Mars Sample Return Orbiter," *Atmospheric Flight Mechanics Conference*, Denver, CO, 2000. <https://doi.org/10.2514/6.2000-4116>.
- [30] Hamel, J.-F., and de Lafontaine, J., "Improvement to the Analytical Predictor-Corrector Guidance Algorithm Applied to Mars Aerocapture," *Journal of Guidance, Control, and Dynamics*, Vol. 29, No. 4, 2006, pp. 1019–1022. <https://doi.org/10.2514/1.20126>.
- [31] Cihan, I. H., and Kluever, C. A., "Analytical Earth-Aerocapture Guidance with Near-Optimal Performance," *Journal of Guidance, Control, and Dynamics*, Vol. 44, No. 1, 2021, pp. 45–56. <https://doi.org/10.2514/1.G005229>, URL <https://doi.org/10.2514/1.G005229>.
- [32] Chen, J., Qiao, D., and Han, H., "Augmented Analytical Aerocapture Guidance by Segmented State Approximation," *Journal of Guidance, Control, and Dynamics*, Vol. 47, No. 10, 2024, pp. 2182–2193. <https://doi.org/10.2514/1.G008322>, URL <https://doi.org/10.2514/1.G008322>.
- [33] Miele, A., Wang, T., Lee, W., and Zhao, Z., "Optimal trajectories for the aeroassisted flight experiment," *Acta Astronautica*, Vol. 21, No. 11, 1990, pp. 735–747. [https://doi.org/https://doi.org/10.1016/0094-5765\(90\)90116-3](https://doi.org/https://doi.org/10.1016/0094-5765(90)90116-3).

- [34] Martin, J., *Atmospheric Reentry: Introduction to its Science and Engineering*, Prentice-Hall Series in Space Technologies, Prentice-Hall, New Jersey, 1966.
- [35] Rumynskii, A., and Churkin, V., “The hypersonic flow of a viscous radiating gas about blunt bodies,” *USSR Computational Mathematics and Mathematical Physics*, Vol. 14, No. 6, 1974, pp. 173–189. [https://doi.org/10.1016/0041-5553\(74\)90178-5](https://doi.org/10.1016/0041-5553(74)90178-5).
- [36] Brandis, A. M., and Johnston, C. O., “Characterization of Stagnation-Point Heat Flux for Earth Entry,” *45th AIAA Plasmadynamics and Lasers Conference*, Atlanta, GA, 2014. <https://doi.org/10.2514/6.2014-2374>.
- [37] Suttles, J. T., Sullivan, E. M., and Margolis, S. B., “Curve fits of predicted inviscid stagnation-point radiative heating rates, cooling factors, and shock standoff distances for hyperbolic Earth entry,” Tech. rep., NASA, 1974.
- [38] Detra, R. W., and Hidalgo, H., “Generalized heat transfer formulas and graphs for nose cone re-entry into the atmosphere,” *Journal of the American Rocket Society*, Vol. 31, No. 3, 1961, pp. 318–321. <https://doi.org/10.2514/8.5471>.
- [39] Tauber, M. E., Palmer, G. E., and Prabhu, D. K., “Stagnation point radiative heating relations for Venus entry,” Tech. rep., 2012.
- [40] Leslie, F., and Justus, C., “The NASA Marshall Space Flight Center Earth Global Reference Atmospheric Model—2010 Version,” Tech. Rep. NASA TM-2011-216467, 2011.
- [41] Bibb, K. L., Walker, E. L., Brauckmann, G. J., and Robinson, P. E., “Development of the Orion Crew Module Static Aerodynamic Database, Part II: Subsonic/Supersonic,” *29th AIAA Applied Aerodynamics Conference*, Honolulu, HI, 2011. <https://doi.org/10.2514/6.2011-3507>.
- [42] Moss, J., Glass, C., and Greene, F., “DSMC Simulations of Apollo Capsule Aerodynamics for Hypersonic Rarefied Conditions,” *9th AIAA/ASME Joint Thermophysics and Heat Transfer Conference*, San Francisco, CA, 2006. <https://doi.org/10.2514/6.2006-3577>.
- [43] Lafleur, J., “The Conditional Equivalence of  $\Delta V$  Minimization and Apoapsis Targeting in Numerical Predictor-Corrector Aerocapture Guidance,” Tech. Rep. NASA TM-2011-216156, 2011.